Monte Carlo based modeling of carbon nanostructured surfaces

Tim C. Petersen, Ian K. Snook, Irene Yarovsky, and Dougal G. McCulloch
Applied Physics, RMIT University, GPO Box 2476V Melbourne 3001, Australia
(Received 22 July 2005; published 13 September 2005)

We have developed Monte Carlo based algorithms to produce realistic models of complex carbon nanostructures with nontrivial curvature, including fullerene junctions between nanotubes. The models are constructed by first analytically defining curved surfaces and then optimizing the configuration of carbon atoms on these surfaces using a realistic interatomic potential. We illustrate our method by generating several previously proposed and also new types of structures, which all show realistic physical properties. Our method is not limited to these structures and can be used to generate large models of nanostructured materials with complex surface geometries and porous structure on the nano-scale.

DOI: 10.1103/PhysRevB.72.125417 PACS number(s): 81.05.Uw, 68.65.−k, 02.70.Uu, 61.48.+c

INTRODUCTION

In many low density carbons that exhibit graphite-like features, the presence of curved aromatic sheets is supported by experimental observation. For example, in fullerenes such as Bucky balls and nano-tubes, or more exotic structures like "graphite conical crystals,"[1] the curvature is both consistent and striking.[2–8] These structures usually contain complex features covering wide length scales from a few tenths to hundreds of nanometers. Accurate atomic models which are capable of realistically describing structural features at various length scales simultaneously are difficult to construct.

Theoretical investigations of carbonaceous structures such as carbon fullerenes and negatively curved graphite[9–13] have shown that it is possible to describe the curvature of carbon surfaces in a physically realistic manner. Different forms of graphitic carbon have been classified by curvature alone.[14–17] In particular, many forms of curved carbonaceous materials, with toroidal[18,19] and even zeolite-like structure,[20–22] have been shown to be energetically stable and physically possible.[23–26] Electronic,[27–29] magnetic,[30] thermodynamical,[25] mechanical and vibrational properties of some of these models have also been calculated[31] as well as elastic energies associated with the warping of aromatic sheets.[32] The experimental fabrication of related carbon materials is being investigated through a variety of approaches.[33–39] Indeed, some researchers have actually produced negatively curved "spongy carbon," which consists of three dimensional and inter-connected meso-porous labyrinths of sp^2-bonded carbon.[40,41] By adapting some of the current methods used to model such materials, we have developed algorithms to model nano-pores defined by curved carbon surfaces with sufficient flexibility to describe structural disorder. Our approach is related to the work of Townsend *et al.*[9] and differs from existing methods for generating such models, which are based on advanced topological and symmetry considerations.[42–46] Other distinct approaches to model carbon nano-pores include molecular dynamics[47] and chemical piecewise construction.[48]

To theoretically describe the structure of curved materials at the atomic scale, the concept of embedding atoms onto curved surfaces has been found to be very useful.[49–51] Using this concept, three dimensionally periodic, curved atomic surface structures may be generated using hyperbolic tiling and symmetry considerations alone. Holyst *et al.*[52,53] recently developed a general algorithm for theoretically describing diffusion of single atoms on curved surfaces, which uses Monte Carlo steps that displace atoms in the local tangent plane of the defining surface and then project the atoms back onto the surface. Following this approach, our paper describes how the confinement of carbon atoms to analytic surfaces can be used as a basis for modeling complex carbon surfaces, with physically realistic bonding.

In this paper we demonstrate our methodology for a range of carbon nano-surfaces. We first detail the construction of carbon models based upon spheres and negatively curved surfaces. Then two other models of fused nano-tubes are presented to demonstrate the flexibility of our approach for modeling structures of specific design, which were inspired by experimental observations reported in the literature.[6]

THEORY

Displacement of points on surfaces

Here we present our original implementation for generating surface structures using concepts first introduced by Holyst *et al.*[53] to model single particle diffusion on membranes. Specifically, we describe Monte Carlo moves on a surface through uniform displacements in the local tangent plane combined with projections back down to the surface,

$$\mathbf{s}_f = \mathbf{s}_i + \mathbf{t} + \mathbf{g} \tag{1}$$

where $\mathbf{s}_i$ and $\mathbf{s}_f$ are vectors denoting the initial and final points on the surface before and after the Monte Carlo move and $\mathbf{t}, \mathbf{g}$ are the tangent and projection vectors, respectively. In this work, we define all surface vectors in terms of Cartesian coordinates,

$$\mathbf{s} = \mathrm{x}\hat{\mathbf{i}} + \mathrm{y}\hat{\mathbf{j}} + \mathrm{z}(\mathrm{x},\mathrm{y})\hat{\mathbf{k}} \tag{2}$$

where $\hat{\mathbf{i}}, \hat{\mathbf{j}}$, and $\hat{\mathbf{k}}$ are unit vectors and $z(x,y)$ is an explicit function of the x and y coordinates. For ease of notation, we further define a surface function

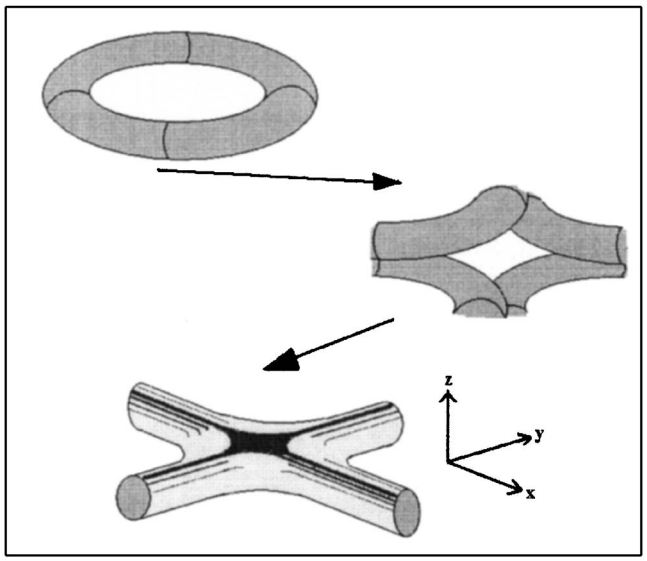

FIG. 1. The geometric scheme used to generate the inverted torus as described in the text.

$$\phi(\mathbf{s}) - c = z(x,y) = 0 \tag{3}$$

where c is a scalar constant.

The tangent vector $\mathbf{t}$ in Eq. (1) is defined by

$$\mathbf{t} = \Delta_x \frac{\dfrac{\partial \mathbf{s}_i}{\partial x}}{\left|\dfrac{\partial \mathbf{s}_i}{\partial x}\right|} + \Delta_y \frac{\left(\dfrac{\partial \mathbf{s}_i}{\partial y}\left|\dfrac{\partial \mathbf{s}_i}{\partial x}\right|^2 - \dfrac{\partial \mathbf{s}_i}{\partial x}\dfrac{\partial \mathbf{s}_i}{\partial x}\bullet\dfrac{\partial \mathbf{s}_i}{\partial y}\right)}{\left|\dfrac{\partial \mathbf{s}_i}{\partial y}\left|\dfrac{\partial \mathbf{s}_i}{\partial x}\right|^2 - \dfrac{\partial \mathbf{s}_i}{\partial x}\dfrac{\partial \mathbf{s}_i}{\partial x}\bullet\dfrac{\partial \mathbf{s}_i}{\partial y}\right|} \tag{4}$$

where Δ_x and Δ_y are the Monte Carlo displacements in the x and y directions, respectively.

The explicit form of the tangent vector $\mathbf{t}$ here ensures that the step size in the tangent plane $|\mathbf{t}| = \sqrt{\Delta_x^2 + \Delta_y^2}$ is randomly selected from a uniform distribution of desired maximum length and the direction of displacement is random. The vector $\mathbf{g}$, which projects a displaced point from the tangent plane back to the surface at $\mathbf{s}_f$, is given by

$$\mathbf{g} = \{c - \phi(\mathbf{s}_i + \mathbf{t})\}\frac{\nabla\phi(\mathbf{s}_i + \mathbf{t})}{|\nabla\phi(\mathbf{s}_i + \mathbf{t})|^2} \tag{5}$$

The form of the projection vector $\mathbf{g}$ was derived from a first-order Taylor expansion of $\phi(\mathbf{s})$, which is valid for small Monte Carlo step sizes relative to the local surface curvature.[53] Further details are given in the Appendix.

Surface definitions

The p-surface

Three dimensionally periodic surfaces offer a computationally convenient means of modeling interconnected pore structure. A simple surface defined by

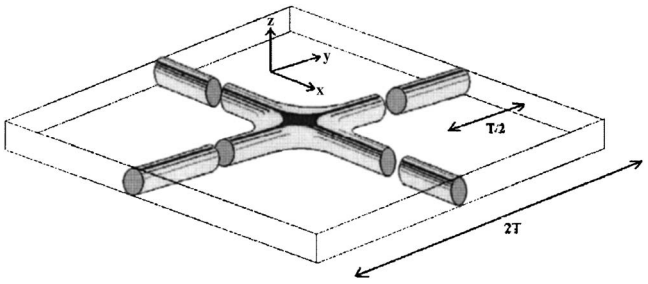

FIG. 2. The inverted torus shown in Fig. 1 analytically joined to four nano tubes in a planar configuration.

$$\phi(\mathbf{s}) = \sum_{i=1}^{3} \cos(2\pi x_i/T) = c \tag{6}$$

is a parameterization of a Fourier approximation[54,55] to Schwarz's "p-surface"[56] and was chosen as a first test for our carbon surface modeling. For simplicity we refer to this surface hereafter as a "p-surface." Equation (2) then becomes

$$\mathbf{s} = x\hat{\mathbf{i}} + y\hat{\mathbf{j}} + \frac{T}{2\pi}\cos^{-1}\left(c - \cos\left(\frac{2\pi x}{T}\right) - \cos\left(\frac{2\pi y}{T}\right)\right)\hat{\mathbf{k}} \tag{7}$$

We generate simple-cubic periodic boundary conditions by varying x_i in Eq. (6) between 0 and T. The areas of surfaces defined by Eq. (6) can be estimated by summing contributions from area elements defined by tangent vectors $\mathbf{t}_x$ and $\mathbf{t}_y$ on the surface

$$\mathrm{A(c,T)} = 8\int_0^{T/2}\int_0^{T/2} |\mathbf{t}_x \times \mathbf{t}_y|\mathrm{dxdy} \cong \sum_{m=1}^{N}\sum_{n=1}^{N} \Delta x \Delta y \times \sqrt{\left(\frac{\delta z(m\Delta x, n\Delta y)}{\delta x}\right)^2 + \left(\frac{\delta z(m\Delta x, n\Delta y)}{\delta y}\right)^2 + 1} \tag{8}$$

where $\Delta x = \Delta y = T/N$ and the form of $z(x,y)$ is given in Eq. (7). Using large values of N, Eq. (8) was used to calculate approximate areas for all p-surfaces defined by Eq. (6).

The sphere

To model spheres of radii R and surface area $A = 4\pi R^2$, centred within a cubic cell of length T, we use

$$\phi(\mathbf{s}) = (x - T/2)^2 + (y - T/2)^2 + (z - T/2)^2 = R^2 = c \tag{9}$$

The coordinates $(x - T/2)$ and $(y - T/2)$ are restricted between $-R/2$ and $R/2$, with $R < T$.

The p-sphere

With an appropriate choice of the parameter c in Eq. (6), the p-surface can be used to accurately approximate the sphere without any further modification. Consider the case where c has a value close to three, such that x_i coordinates satisfying Eq. (6) must cause each cosine to attain its maximum value of one. For such values of c, Taylor expansions

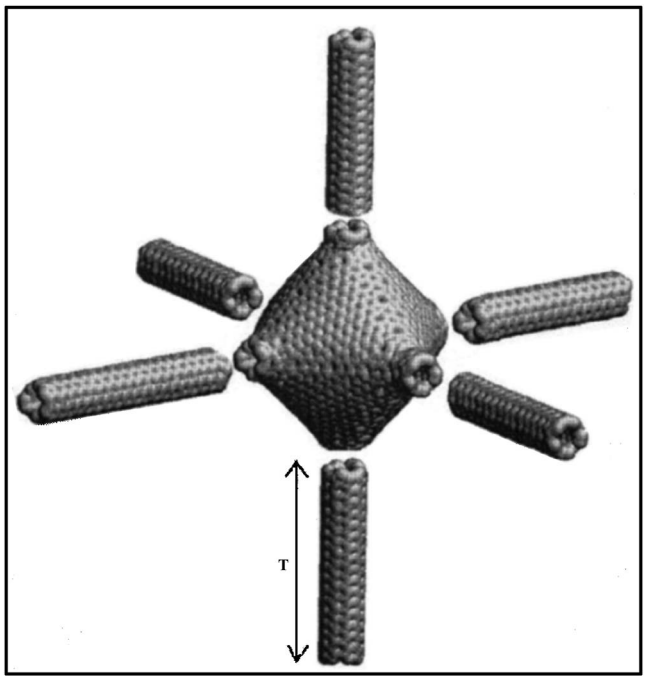

FIG. 3. Three-dimensionally fused nano-tubes can be modeled using the *p*-surface of Eq. (6) with appropriate choices for *c* and *T* as an interior junction to which six nano-tubes can be smoothly attached.

of the cosines about $x_i=0$ can be accurately truncated to first order such that $\phi(\mathbf{s}) \cong 3-\Sigma_{i=1}^{3}(2\pi x_i/T)^2/2! = c$. Rearranging gives:

$$x^2 + y^2 + z^2 = R^2 \cong 2(T/2\pi)^2(3-c) \tag{10}$$

Employing the same cubic periodic boundary conditions as for the *p*-surface, Eq. (10) describes a sphere split into eight segments at the edges of the periodic boundaries. Each of these segments can be re-combined by simply translating all *p*-sphere cell boundaries by $T/2$ and reapplying the periodic boundary conditions. It should be noted that Eq. (10) still represents the *p*-surface, which has an Euler characteristic of negative four, whereas the sphere possesses no topological handles and, therefore, has an Euler characteristic of two.

The inverted torus

To generate a junction model for fusing nano-tubes, we construct a quarterized torus, invert it about its center and cap it top and bottom with planar surfaces (see Fig. 1). Specifying the inner and outer torus radii by the parameters *a* and *c*, respectively, the mathematical form of the inverted torus in Fig. 1 is

$$\begin{aligned}\phi(\mathbf{s}) &= \left(c - \sqrt{\left(x_{pq}-\frac{T}{2}\right)^2 + \left(y_{pq}-\frac{T}{2}\right)^2}\right)^2 + \left(z_{pq}-\frac{T}{2}\right)^2 - a^2 \\ &= 0, \text{ for } |\mathbf{s}_{pq}| < (a^2-c^2) \\ &= \left(z_{pq}-\frac{T}{2}\right) - a\frac{\left(z_{pq}-\frac{T}{2}\right)}{\left|z_{pq}-\frac{T}{2}\right|} = 0, \text{ for } |\mathbf{s}_{pq}| > (a^2-c^2)\end{aligned} \tag{11}$$

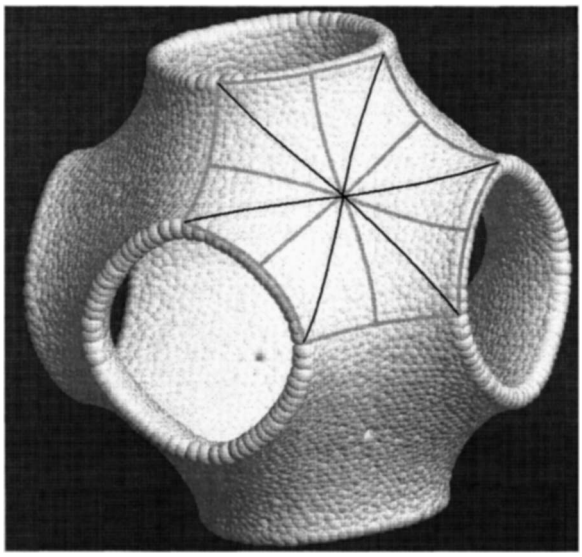

FIG. 4. The *p*-surface of Eq. (6) broken into 96 identical surface elements. To improve the inter-atomic bonding near the junctions of the elements, the number of imposed symmetry operations was halved, creating surface elements marked by the grey lines only.

where $\mathbf{s}_{pq}=\mathbf{s}-(px\hat{\mathbf{i}}+qy\hat{\mathbf{j}})+T/2\hat{\mathbf{k}}$, and p, $q=0$ or 1. The (x,y,z) coordinates were again restricted between 0 and T, to create an infinite two dimensional lattice of connected inverted tori via imposed periodic boundary conditions. The surface area A_{fused} of this structure is

$$A_{fused} = 2\pi^2 ac - 4\pi a^2 + 2T^2 - 2\pi c^2 \tag{12}$$

Planar fused nano-tubes

Four nano-tubes can now be attached to the inverted torus which is analytically described at the boundaries $(x-T/2, y-T/2)=(\pm T/2, \pm T/2)$ by cylinders. This generates a model comprised of four fused nano-tubes in a planar configuration as illustrated in Fig. 2, where the nanotubes were designed to be half the length of the inverted torus junction defined by T in Eq. (11).

Three-dimensional fused nano-tubes

Another suitable nano-tube junction is the *p*-surface sliced along its cubic boundaries since, for a particular value of *c*, these surface cross sections can be accurately described by circles. Consider the $x-y$ plane cross section, where $z=0$. Equation (6) then becomes:

$$\phi(x,y,z=0) - 1 = \cos(2\pi x/T) + \cos(2\pi y/T) = c - 1 \cong -2 \tag{13}$$

Equation (13) requires that each cosine have value close to negative one. The cosines can then be approximated by Taylor expansions about x and $y=T/2$ to give:

$$(x-T/2)^2 + (y-T/2)^2 \cong \left(\frac{T}{2\pi}\sqrt{2(c+1)}\right)^2 \tag{14}$$

Equation (14) shows that the *p*-surface of Eq. (6) can be described by a circle centerd in the $x-y$ plane with radius

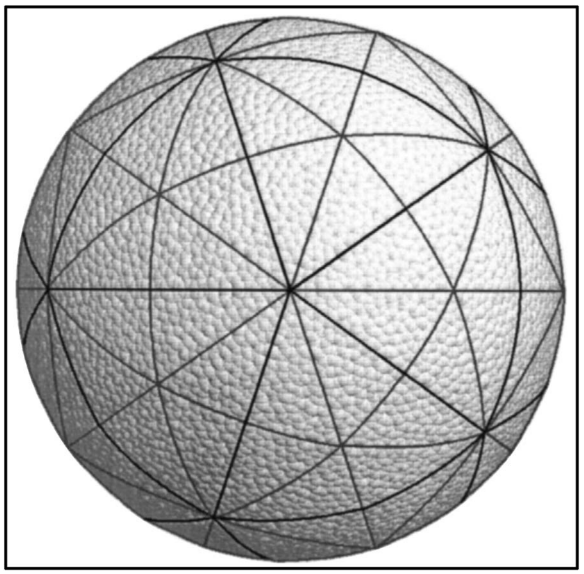

FIG. 5. The symmetries of the icosahedron applied to the sphere to create 120 irreducible elements. To reduce unphysical bonding near the junctions of the elements for smaller systems, the number of enforced symmetry operations was decreased to 60, thereby redefining the irreducible surface elements to be marked by the grey lines only.

controlled by T and c. Similar arguments follow for all cross sections for which one of the coordinates x_i in Eq. (6) is equal to zero. Through appropriate choices of c and T, the p-surface can, therefore, be designed to provide a cubic junction to which six nano-tubes can be smoothly attached, as depicted in Fig. 3.

For the three-dimensional fused nanotube structure modeled in this work, the length of the nanotubes attached to the central p-surface of Eq. (6) were set equal to the length T of the junction, as shown in Fig. 3.

Imposing surface symmetry

Subdividing large systems into smaller identical pieces can vastly improve computational efficiency, regardless to whether symmetries in structural models are desired. To demonstrate the application of symmetry in the context of this work, we have imposed a variety of symmetries upon the p-surface, sphere and fused torus. Details of the mathematics and algorithm used to impose these symmetries are provided in the Appendix.

Figure 4 shows how the p-surface of Eq. (6) (using $c=0$) can be broken into 96 surface elements defined by the boundaries of the black and grey lines. It is clear that the imposition of this symmetry can lead to unusual bonding effects near the junctions of the boundaries. To diminish unphysical bonding effects in these regions for smaller systems, the imposed symmetry operations were relaxed to give only 48 irreducible elements, which are marked by the grey lines in Fig. 4. It should be noted that the black lines do not represent surface symmetries of Eq. (6) when $c \neq 0$.

Based on the symmetry of C_{60}, we also imposed the symmetry of the icosahedron on the sphere, as depicted in Fig. 5,

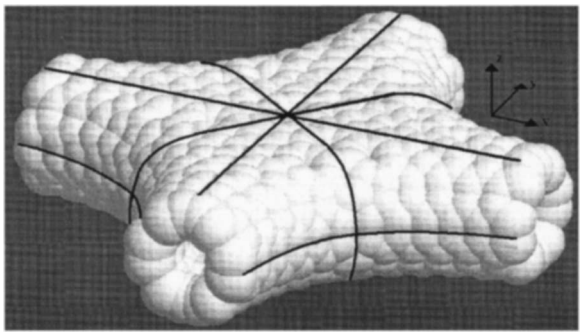

FIG. 6. Symmetry imposed on the fused torus used to divide the surface into 16 identical elements.

which shows the sphere broken into 120 identical elements. Again, fewer symmetry operations were enforced for smaller models, thereby creating just 60 irreducible elements defined by the grey lines in Fig. 5.

Finally, the fused torus was broken into 16 identical elements as shown in Fig. 6.

The Monte Carlo surface algorithm

Using Eqs. (1), (4), and (5) to advance an atom along the surface by a small step size, the energy associated with the atom move is calculated using an interaction potential as a function of the Euclidean inter-atomic separation of atoms. As with any Monte Carlo simulation, the quality of the resulting structure depends largely on that of the inter-atomic potential.[57] In this work we employed the Environment Dependent Interaction Potential (EDIP), which was originally developed by Justo *et al.*[58] for Silicon. Marks[59] later adapted EDIP to provide a good physical description of carbon bonding.[60] Moves that improve the energy of the system are accepted outright and all other moves are accepted with the conditional probability $P=e^{-\Delta E/kT}$, where kT is the Boltzmann weighting factor and ΔE is the difference in the energy of the system caused by the proposed Monte Carlo move.

Symmetries were imposed by applying symmetry operations to the coordinates of unique atoms on the surface to generate the coordinates of all other atoms. Rather than replicate all of the nonunique positions at each Monte Carlo step, lists were constructed within the algorithm code to re-

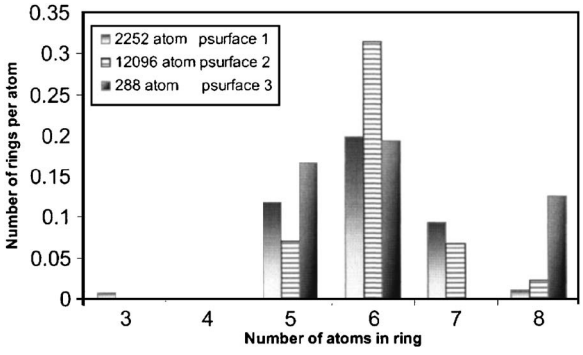

FIG. 7. Ring statistics for all of the optimized p-surface models listed in Table I.

TABLE I. Details of the various calculations conducted to demonstrate the application of the carbon surface modeling algorithm.

Model name	Number of atoms	Symmetry	Specific details
p-surface 1	2252	None	c in Eq. (6) set to 0, $T=50$ Å
p-surface 2	12096	96	c in Eq. (6) set to 0, $T=116$ Å
p-surface 3	288	48	c in Eq. (6) set to 0, $T=17.9$ Å
sphere 1	12000	120	Radius set to 50 Å
sphere 2	840	60	Radius set to 13.2 Å
sphere 3	240	60	Radius set to 7.06 Å
p-sphere	816	48	c in Eq. (6) set to 2.99, $T=578.61$ Å
Planar fused tubes	1320	16	Symmetry applied to central inverted torus then later removed. Nanotube type (5,5). Torus parameters: $a=3.438$ Å, $c=20$ Å, $L_{\text{tube}}=T/2=20$ Å
Three dimensional fused tubes	3984	48	Symmetry applied to the central *p*-surface then later removed. Nanotube type (5,5). c Eq. (6) set to −0.9, $T=48.3$ Å $L_{\text{tube}}=20$ Å

late each unique atom to its various symmetrically equivalent partners. In this manner, computational efficiency was increased and new symmetries were implemented by simply modifying the replication and symmetric list procedures, instead of modifying all functions dependent upon the local atomic structure. Further details are given in the Appendix.

CALCULATION DETAILS

Table I summarizes the nine representative structures modeled. The first seven calculations were performed in order to demonstrate the capabilities of the method to describe physically realistic fullerenes. The last two were designed to show how our method can be used to model more complex structures which bare some resemblance to experimental observations.[6,61]

Nanotube structures of type (5, 5)[62] with radii 3.438 Å and 150 atoms each were used in both of the fused nanotube models. For all other surfaces, the number of atoms was determined by making the surface density ρ of each model the same as that of the basal plane of graphite $\rho \cong 0.3829$ atoms/Å^2. Cubic periodic boundary conditions were used for all systems.

To prepare each structure, atoms were placed randomly within the periodic boundaries and those which satisfied Eq. (6) to within a small tolerance were accepted as initial surface atoms. For the *p*-surface and sphere models, the initial structures were then annealed in separate stages starting at $T=5000$ K and halving this temperature between each stage until $T=300$ K. For the fused tube models, the same procedure was applied to the interior junction surfaces, with symmetry constraints also imposed. After minimization of the energy, these junctions were joined to the nano-tubes and the symmetry constraints removed in order to model the fused structures. Annealing was again applied to remove the unphysical bonding that resulted from the initial joining. Trial calculations on the larger models indicated that step sizes producing a 20% acceptance probability reduced the total energy most rapidly.

RESULTS

Table II shows the cohesive energies and coordination

TABLE II. Cohesive energies and three fold coordination fractions for all of the carbon nano-surfaces modeled.

Model name	Final cohesive energy (eV/atom) (Graphite: 7.36)	Fraction of threefold coordinated atoms
p-surface 1	7.15	96%
p-surface 2	7.10	99%
p-surface 3	7.00	100%
sphere 1	6.71	95%
sphere 2	6.96	100%
sphere 3	7.20	100%
p-sphere	6.99	100%
Planar fused tubes	6.74	95%
Three dimensional fused tubes	6.93	99%

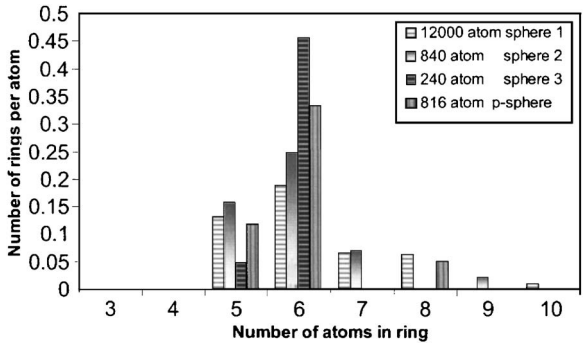

FIG. 8. Ring size distributions for the sphere models listed in Table I.

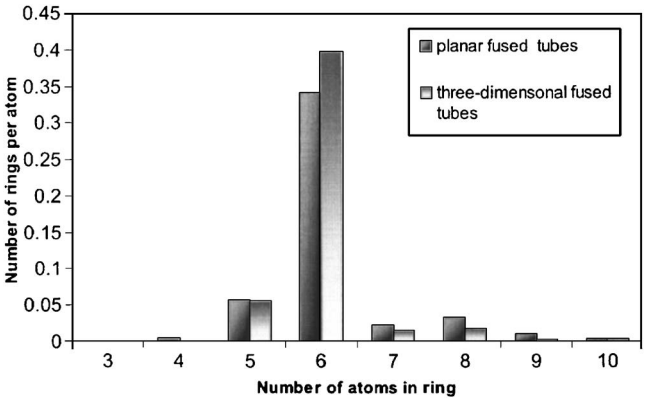

FIG. 9. Ring size distributions for the fused nano-tube models listed in Table I.

fractions for the final atomic configurations of each of the carbon nano-surfaces listed in Table I, calculated using a coordination radius of 1.85 Å. The EDIP energy per atom calculated for the graphite structure is also provided in Table II as a reference. In every model, the only remaining coordination types were twofold and all models show a high degree of desired threefold (aromatic) bonding on the nano-surfaces.

The energy of sphere 1 indicates that the 120 icosahedron symmetry elements were too severe, causing unphysical bonding effects. Spheres 2 and 3, with only 60 imposed symmetry elements, have a more physical structure. Like sphere 1, the planar fused tubes model exhibits relatively poor energy and coordination. The *p*-sphere results show that it is possible to construct large energetically favorable Bucky balls with octahedral symmetry and optimal threefold connectivity.

The poorer physical quality of the planar fused tube model may have resulted from the initial imposed symmetries that were incommensurate with both aromatic bonding and the symmetry of the nano-tubes. Relative to the planar model, the three-dimensional fused tubes display better overall properties.

Ring statistics for *p*-surfaces 1, 2 and 3, calculated using Franzblau's shortest path criterion[63] and a maximum bond length of 1.85 Å, are shown in Fig. 7, which displays a range of ring types centerd about six, with the smaller models containing broader distributions. A very small number of twelve member rings for *p*-surface 2 have been omitted for clarity.

Interestingly, *p*-surface 1 also contains a small percentage of strained three-member rings, which contrasts with the good cohesive energy reported in Table II.

Figure 8 displays the ring distributions for the sphere and *p*-sphere models with the largest model showing the broadest distribution. The relative spread of the ring distribution and outlying numbers of ten-member rings for sphere 1 are a direct result of the larger number of symmetry elements imposed, which conflict with carbon bonding. The *p*-sphere is shown to contain a significant number of eight member rings, as expected from the imposed octahedral symmetry.

The planar fused nano-tube results in Fig. 9 show a slightly broader distribution and a small number of strained four-member rings, which correlate with the poorer cohesive energy reported in Table II.

Figures 10–12 display the connectivity of an atomic configuration for each of the *p*-surface models. While Table II reports a good cohesive energy for *p*-surface 1, Fig. 10 indicates that there are a number of rings and bonds distorted from ideal configurations, though the structure is largely aromatic. Figure 11 very clearly shows how the imposed symmetries affect the bonding in the vicinity of some regions. For example, surrounding the largest (twelve member) rings, other large rings and four member rings are visible. In order to better display the interconnected bonding of *p*-surface 3, Fig. 12 shows a small section of this model repeated in two directions, which looks much like the 216 atom model of Townsend *et al.*[9]

Figure 13 again indicates that imposing too many or inappropriate symmetry elements can cause conflicts with aromatic bonding. Although the 840 atom sphere 2 model contains a significant number of large rings, Fig. 14 shows that the bonds in these rings are largely sp^2-like in nature, which explains the good cohesive energy reported in Table I. Figure 15 shows that the 240 atom sphere is comprised of aromatic type bonds, much like the structure of C_{60} and resembles the 240 fullerene model discussed by Kroto.[43] Figure 16 indicates that the octahedral symmetries imposed on the 816

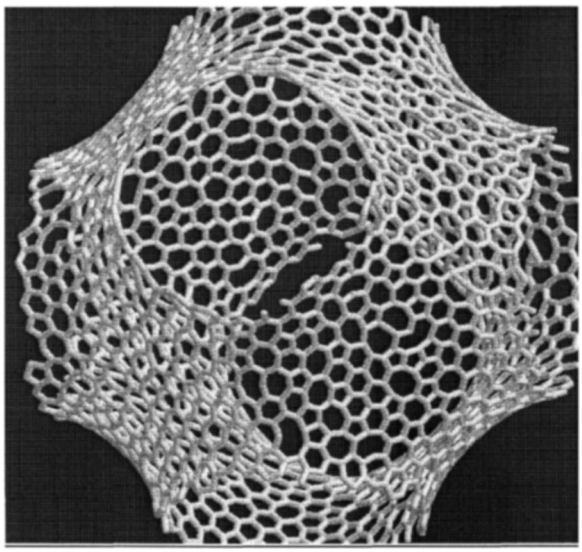

FIG. 10. One atomic configuration representing *p*-surface 1 with no imposed symmetry.

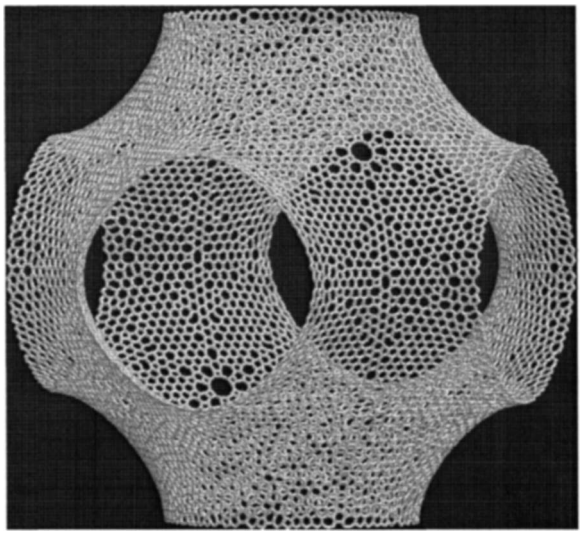

FIG. 11. A view of the 12 096 atom model *p*-surface 2, clearly showing the imposed symmetry.

atom *p*-sphere can produce bonding configurations similar to spheres with conventional icosahedral symmetry.

Figures 17 and 18 show configurations of the fused nanotube atomic networks where the smooth bonding of the nanotubes to the central junctions is evident. The planar fused nano-tubes in Fig. 17 display some stretched bonding, corresponding to the higher twofold coordination fractions and low cohesive energy in Table II. Figure 18 indicates that much of the symmetry applied to the central *p*-surface junction has been preserved after energetic annealing, because a good cohesive energy was obtained before fusing the nanotubes. Both the models in Figs. 17 and 18 contained small numbers of twofold coordinated atoms.

CONCLUSION

This paper has shown that a variety of physically realistic carbon nano-surfaces can be constructed by modeling the interaction of carbon atoms on analytically defined surfaces. It was also shown how symmetry can be used to create large

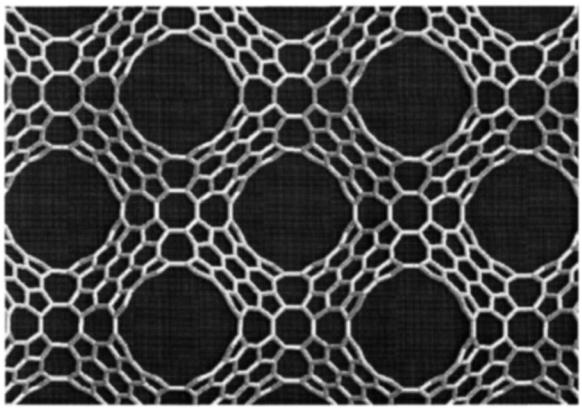

FIG. 12. A projection of the *p*-surface 3 structure, repeated along two directions.

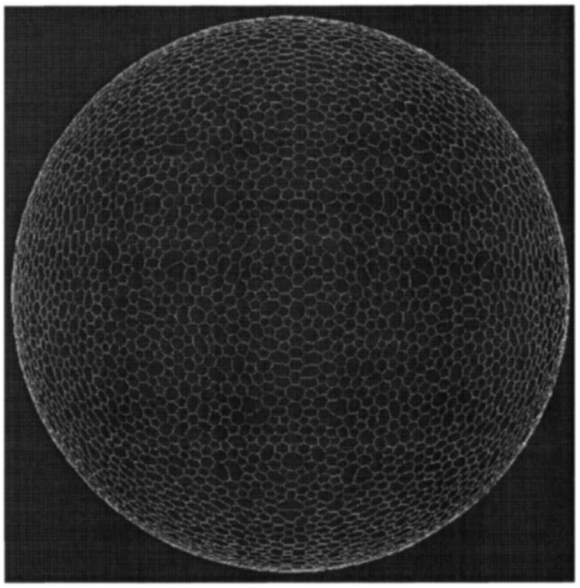

FIG. 13. The giant sphere 1 containing 12 000 atoms contains some regions with undesirable bonding effects due to over-imposed symmetry.

atomic model structures with a high degree of aromatic bonding. Two different and physically realistic models of fused nano-tubes were constructed to further demonstrate the surface modelling algorithm applied to surfaces of specific design, which were inspired from experimental investigations reported in the literature.[6,61]

The novelty and utility of our approach is related to the manner in which large models can be constructed with sufficient flexibility to describe a whole range of low energy structures; even those containing structural disorder. The algorithms reported here may be extended to describe very large nano-porous carbonaceous models that also adhere to experimental observations in a variety of ways. Relaxation of

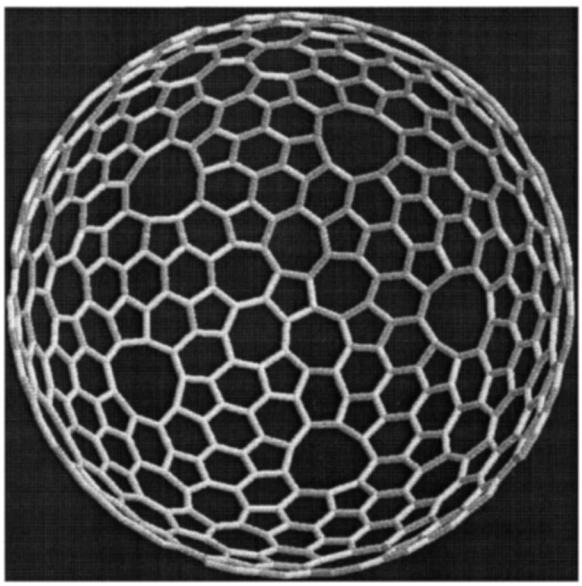

FIG. 14. Inside portion for an atomic configuration of the sphere 2 model.

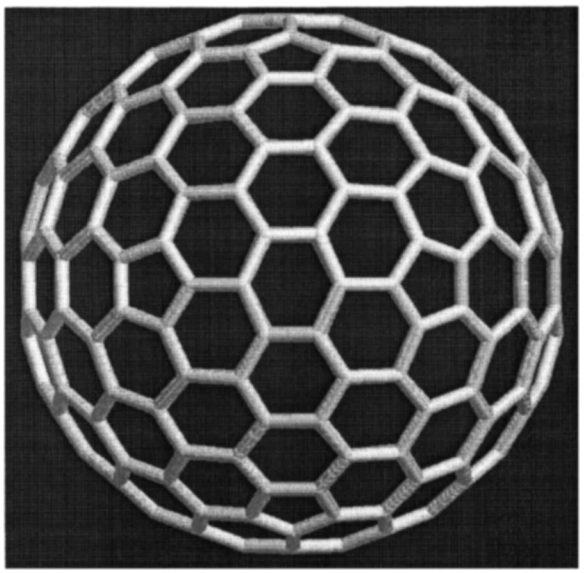

FIG. 15. Atomic configuration for sphere 3 model, comprised of just four unique atoms.

structures without surface constraints and models with different surface densities or omitted symmetry elements may also be investigated to produce improved structures.

ACKNOWLEDGMENTS

The authors would like to thank Dr. Nigel Marks for use of his EDIP energy code and Dr. Brendan O'Malley for his ring statistics code. The authors would also like to thank the Australian Partnership for Advanced Computing (APAC) and the Victorian Partnership for Advanced Computing (VPAC) for providing computer time for the calculations presented here.

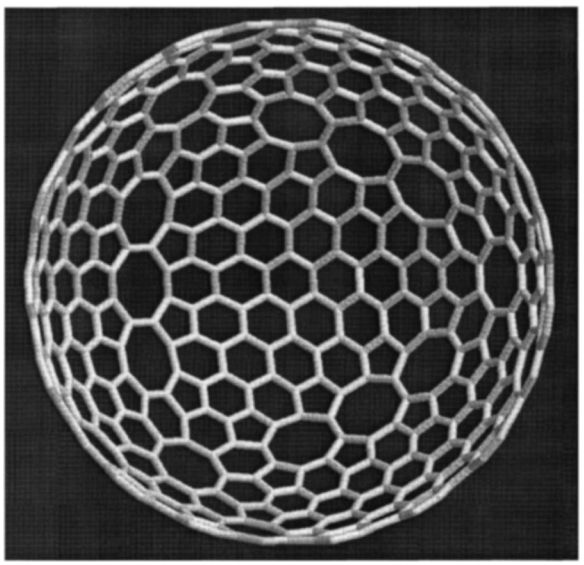

FIG. 16. Inside portion for an atomic configuration of the *p*-sphere model.

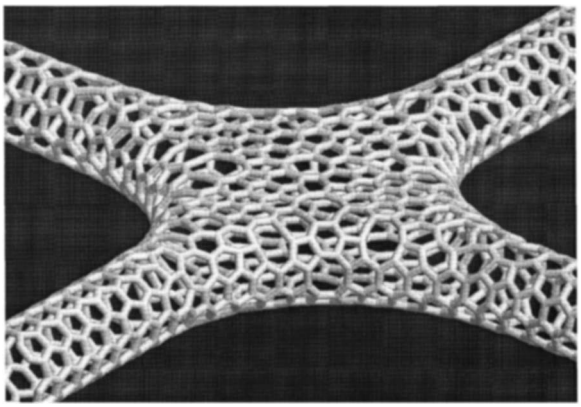

FIG. 17. Atomic bonding configuration for the planar fused nano-tube model listed in Table I.

APPENDIX

The tangent and projection vectors

Consider a point on the surface described by the vector **s**:

$$\mathbf{s} = x\hat{\mathbf{i}} + y\hat{\mathbf{j}} + z\hat{\mathbf{k}} = x\hat{\mathbf{i}} + y\hat{\mathbf{j}} + f(x,y)\hat{\mathbf{k}}, \tag{A1}$$

where $f(x,y) - z = \phi(s) - c = 0$. Two vectors in the tangent plane of the surface at an initial point **s** are, for example:

$$\frac{\partial \mathbf{s}}{\partial x} = \hat{\mathbf{i}} + \frac{\partial z}{\partial x}\hat{\mathbf{k}} = \hat{\mathbf{i}} + \frac{\partial \mathrm{f}(x,y)}{\partial \mathrm{x}}\hat{\mathbf{k}} \text{ and } \frac{\partial \mathbf{s}}{\partial y} = \hat{\mathbf{j}} + \frac{\partial \mathrm{f(x,y)}}{\partial \mathrm{y}}\hat{\mathbf{k}}$$

These tangent vectors can be generalized to an arbitrary tangent vector **t**:

$$\mathbf{t} = \Delta_x \frac{\dfrac{\partial \mathbf{s}}{\partial x}}{\left|\dfrac{\partial \mathbf{s}}{\partial x}\right|} + \Delta_y \frac{\dfrac{\partial \mathbf{s}}{\partial y}}{\left|\dfrac{\partial \mathbf{s}}{\partial y}\right|} = \Delta_x \mathbf{u} + \Delta_y \mathbf{v} \tag{A2}$$

Where Δ_x and Δ_y specify the relative contributions of the unit tangent vectors **u** and **v** respectively. For Monte Carlo simulation, increments in the tangent plane must be selected from a distribution of desired step size, with unbiased direction. For the Δ_x and Δ_y in Eq. (A2) selected from a uniform distribution, these two requirements specify that:

$$|\mathbf{t}|^2 = \Delta_x^2 + \Delta_y^2 \text{ and } \mathbf{u}\bullet\mathbf{v} = 0$$

Both of these conditions can be satisfied by Gram-Schmidt orthogonalization[64] of **u** and **v**: $\mathbf{v} \rightarrow \frac{\mathbf{v}-\mathbf{u}(\mathbf{u}\bullet\mathbf{v})}{|\mathbf{v}-\mathbf{u}(\mathbf{u}\bullet\mathbf{v})|}$, which gives

$$\mathbf{t} = \Delta_x \frac{\dfrac{\partial \mathbf{s}}{\partial x}}{\left|\dfrac{\partial \mathbf{s}}{\partial x}\right|} + \Delta_y \frac{\left(\dfrac{\partial \mathbf{s}}{\partial y} - \dfrac{\partial \mathbf{s}}{\partial x}\dfrac{\partial \mathbf{s}}{\partial x}\bullet\dfrac{\partial \mathbf{s}}{\partial y}\right)}{\left|\dfrac{\partial \mathbf{s}}{\partial y} - \dfrac{\partial \mathbf{s}}{\partial x}\dfrac{\partial \mathbf{s}}{\partial x}\bullet\dfrac{\partial \mathbf{s}}{\partial y}\right|} \tag{A3}$$

Having displaced an atom in the tangent plane, the atom must be projected back onto the surface. For small displacements in the tangent plane, the required projection vector **g** can be determined by Taylor expanding $\phi'(\mathbf{s}) = \phi(\mathbf{s}) - c$ about the initial atom position $\mathbf{s}_i$:

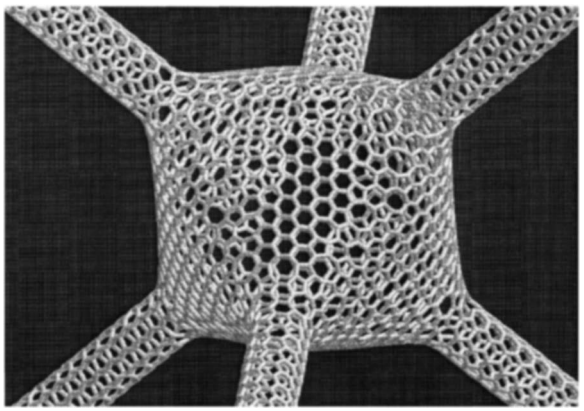

FIG. 18. Atomic bonding configuration for the three-dimensional fused nano-tube model listed in Table I.

$$\phi'(\mathbf{s}_i + \{\mathbf{t} + \mathbf{g}\}) = \phi'(\mathbf{s}_i) + (\mathbf{t} + \mathbf{g}) \bullet \nabla \phi'(\mathbf{s}_i) + \cdots \quad \text{(A4)}$$

Likewise:

$$\phi'(\{\mathbf{s}_i + \mathbf{t}\} + \mathbf{g}) = \phi'(\mathbf{s}_i + \mathbf{t}) + \mathbf{g} \bullet \nabla \phi'(\mathbf{s}_i + \mathbf{t}) + \cdots \quad \text{(A5)}$$

For small displacements, Eqs. (A4) and (A5) truncated to first order give:

$$\phi'(\mathbf{s}_i + \mathbf{t}) + \mathbf{g} \bullet \nabla \phi'(\mathbf{s}_i + \mathbf{t}) = \phi'(\mathbf{s}_i) + (\mathbf{g} + \mathbf{t}) \bullet \nabla \phi'(\mathbf{s}_i)$$

rearranging gives:

$$\mathbf{g} = \frac{\{\phi'(\mathbf{s}_i) - \phi'(\mathbf{s}_i + \mathbf{t}) + \mathbf{t} \bullet \nabla \phi'(\mathbf{s}_i)\} \nabla \{\phi'(\mathbf{s}_i + \mathbf{t}) - \phi'(\mathbf{s}_i)\}}{|\nabla \{\phi'(\mathbf{s}_i + \mathbf{t}) - \phi'(\mathbf{s}_i)\}|^2} \quad \text{(A6)}$$

Using the definition of the surface equation $\phi'(\mathbf{s}_i) = \phi(\mathbf{s}_i) - c = 0$ and the fact that the tangent vector $\mathbf{t}$ is orthogonal to the normal of the surface $\mathbf{t} \bullet \nabla \phi'(\mathbf{s}_i) = 0$, the projection vector $\mathbf{g}$ then simplifies to

$$\mathbf{g} = \{c - \phi(\mathbf{s}_i + \mathbf{t})\} \frac{\nabla \phi(\mathbf{s}_i + \mathbf{t})}{|\nabla \phi(\mathbf{s}_i + \mathbf{t})|^2} \quad \text{(A7)}$$

Surface symmetry

All imposed symmetries in the surface calculations were implemented by performing symmetry operations on the coordinates of each unique surface atom. In our algorithm, each symmetry operation on a unique atom generates a nonunique partner atom at a symmetrically corresponding point on the surface. Therefore, each proposed Monte Carlo move of a unique atom is accompanied by the symmetrical movement of all its corresponding nonunique partner atoms at all equivalent points on the surface. Likewise, rejection of a proposed Monte Carlo move results in rejection of the move for all symmetric partners. Unlike periodic boundary conditions, which employ the minimal imaging convention,[57] unique atoms are permitted in our algorithm to interact with symmetric partners lying within reach of the inter-atomic potential.

Different symmetries can be imposed on a given surface and each surface requires a different treatment of symmetry. It is expected that, for more complex surfaces, a more rigorous treatment of symmetry would be required by appealing to group theory. The following sections detail the implementation of the symmetries that were chosen to be imposed on the surfaces modeled in this work.

Symmetry imposed on the *p*-surface and *p*-sphere

From inspection of Eq. (6), it is clear that each cosine contains unique values in only one quarter of its cycle determined by the values of the coordinates x, y, and z. Operations on these coordinates that leave each cosine unchanged also leave Eq. (3) unchanged. Such operations, therefore, map a given point to another symmetrically equivalent point on the surface. Likewise, combinations of operations on the cosines in Eq. (6) that leave Eq. (3) unchanged are also symmetry operations. After identifying a number of desired symmetries to be imposed upon a surface, it is important to ensure that different combinations of symmetry operations do not result in identical mappings (overlapping) for the atomic coordinates, thereby producing "degenerate" mappings. For the *p*-surface, degeneracy was avoided by enumerating all unique combinations of chosen symmetry operations. Denoting $\hat{\mathbf{S}}$ as a symmetry operator that acts on a given surface vector $\mathbf{s}$, the symmetries imposed to create the patterned surface patches observed in Fig. 4, without degeneracy, are given by Eq. (A8):

$$\hat{\mathbf{S}}\mathbf{s} = \left\{ \sum_{t=0}^{\tau} \sum_{\alpha=1}^{2} \sum_{\beta=1}^{2} \sum_{\gamma=1}^{2} \sum_{i=1}^{3} \sum_{j \neq i}^{3} \sum_{k \neq j \neq i}^{3} (2\alpha - 3 - Tt/2)\hat{\mathbf{x}}_i + (2\beta - 3 - Tt/2)\hat{\mathbf{x}}_j + (2\gamma - 3 - Tt/2)\hat{\mathbf{x}}_k \right\} \bullet \mathbf{s}$$

where for $c \neq 0, \tau = 0$ otherwise $\tau = 1$ and $\hat{\mathbf{x}}_1 = \hat{\mathbf{i}}, \hat{\mathbf{x}}_2 = \hat{\mathbf{j}}$,

$$\hat{\mathbf{x}}_3 = \hat{\mathbf{k}}, (\mathbf{s} = x\hat{\mathbf{i}} + y\hat{\mathbf{j}} + z\hat{\mathbf{k}}) \quad \text{(A8)}$$

where the parameter τ controls whether or not the black lines in Fig. 4 are present for surfaces with $c = 0$.

Each operation in Eq. (A8), defined by the summation integers and the dot product (•), generates one nonunique atomic coordinate from an atom with coordinates $\mathbf{s}(x, y, z)$. Equation (A8), therefore, produces a total of 96 symmetrically equivalent atomic coordinates, which reduces to 48 for $\tau \neq 1$.

Symmetry imposed on the sphere

A number of symmetries on the sphere can be imposed by inscribing "plutonic solids" such as the pyramid, cube or even the icosahedron within the sphere. Inspection of Fig. 5 indicates that these imposed symmetries can be described by combinations of rotation axes about the vertices of the icosahedron and reflections through planes that contain any two neighboring icosahedron vertices. Inscribed on a sphere of radius R centered at (0,0,0), these 12 vertices $\mathbf{v}_i$ are defined by the golden ratio ϕ:[65]

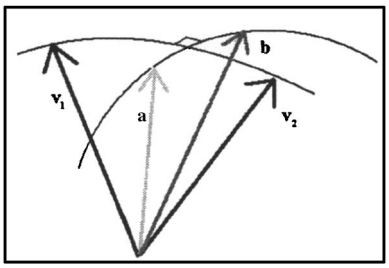

FIG. 19. Given two vectors $\mathbf{v}_1$ and $\mathbf{v}_2$ on the sphere, vector **a** is reflected through the plane containing $\mathbf{v}_1$ and $\mathbf{v}_2$ to become **b**.

$$\mathbf{v}_i(x,y,z) = \left[\frac{R}{\sqrt{1+\phi^2}}(0, \pm\phi, \pm 1), \frac{R}{\sqrt{1+\phi^2}} (\pm 1, 0, \pm\phi), \frac{R}{\sqrt{1+\phi^2}}(\pm\phi, \pm 1, 0) \right] \quad \text{(A9)}$$

where $\phi = \frac{1}{2}(1+\sqrt{5})$ and the subscript i labels each vertex vector.

Figure 19 depicts two such neighboring vertices that can be used to map a surface vector **a** to its symmetrically reflected position **b**.

Geometric analysis can be used to express Fig. 19 mathematically:

$$\hat{\mathbf{F}}(\mathbf{v}_1,\mathbf{v}_2)\begin{bmatrix} a_x \\ a_y \\ a_z \end{bmatrix} = \mathbf{b} = \mathbf{a} - 2\mathbf{a}(\mathbf{v}_1 \times \mathbf{v}_2)\frac{(\mathbf{v}_1 \times \mathbf{v}_2)}{|\mathbf{v}_1 \times \mathbf{v}_2|^2} \quad \text{(A10)}$$

where $\hat{\mathbf{F}}(\mathbf{v}_i, \mathbf{v}_j)$ will be called a "reflection operator" and a_x, a_y, a_z are the components of **a**. Arbitrary rotation of a surface vector **s** about an icosahedron vertex **v** can be described using Cartesian rotation matrices to first align the z axis of the employed coordinate system with the direction of **v**, followed by rotation of **s** about this axis and then reverse alignment of the coordinate system. After combining all of these operations, the resulting rotation operator $\hat{R}(\mathbf{v}_i, \theta_j)$ has the form:

$$\hat{R}(\mathbf{v}_i,\theta_j)\begin{bmatrix} x \\ y \\ z \end{bmatrix} = \begin{bmatrix} \alpha_i^2 c_j + \beta_i^2 & \beta_i\delta_i\alpha_i c_j + \gamma_i\alpha_i s_j - \beta_i\delta_i\alpha_i & -\beta_i\gamma_i\alpha_i c_j + \alpha_i\delta_i s_j + \beta_i\gamma_i\alpha_i \\ \beta_i\delta_i\alpha_i c_j - \alpha_i\gamma_i s_j - \beta_i\delta_i\alpha_i & (\gamma_i^2 + \beta_i^2\delta_i^2)c_j + \alpha_i^2\delta_i^2 & (1-\beta_i^2)\gamma_i\delta_i c_j + (\gamma_i^2+\delta_i^2)\beta_i s_j - \delta_i\alpha_i^2\gamma_i \\ -\beta_i\gamma_i\alpha_i c_j - \alpha_i\delta_i s_j + \beta_i\gamma_i\alpha_i & (1-\beta_i^2)\gamma_i\delta_i c_j - (\gamma_i^2+\delta_i^2)\beta_i s_j - \delta_i\alpha_i^2\gamma_i & (\delta_i^2+\beta_i^2\gamma_i^2)c_j + \alpha_i^2\gamma_i^2 \end{bmatrix}\begin{bmatrix} x' \\ y' \\ z' \end{bmatrix} \quad \text{(A11)}$$

where $\gamma_i = v_{iz}/\sqrt{v_{iy}^2+v_{iz}^2}$, $\delta_i = v_{iy}/\sqrt{v_{iy}^2+v_{iz}^2}$, $\alpha_i = \sqrt{v_{iy}^2+v_{iz}^2}/|\mathbf{v}_i|$, $\beta_i = v_{ix}/|\mathbf{v}_i|$, $|\mathbf{v}_i| = \sqrt{v_{ix}^2+v_{iy}^2+v_{iz}^2}$ and the trigonometric functions $c_j = \cos(2\pi j/5)$, $s_j = \sin(2\pi j/5)$ describe fivefold rotations about $\mathbf{v}_i$ such that $\theta_j = 2\pi/5$. Note that the atomic coordinates x', y', and z' in Eq. (A11) refer to coordinates measured relative to the origin (0,0,0) during application of $\hat{R}(\mathbf{v}_i, \theta_j)$.

Combining the rotation and reflection operations without introducing degeneracy amongst nonunique atoms is not trivial. To avoid the overlapping of these atoms a graph of icosahedron vertices was employed, as shown in Fig. 20.

Figure 20 displays all of the icosahedron vertices labeled 1–12, with vertex 12 obscured from view. It is convenient (though not necessary) to visualize all unique atoms located inside region 1; defined by the boundaries around vertex 1. All symmetrically equivalent atomic positions are generated by first filling out this region and then mapping both the original and generated coordinates to all other symmetrically identical regions. Referring to Fig. 20, this involves first reflecting (represented by the grey arrow) using $\mathbf{v}_1$ and $\mathbf{v}_3$ and then rotating the resulting and original coordinates about vertex 1. After (effectively) filling region 1, all atomic coordinates are then mapped to region 2 via rotation about vertex three. Coordinates in region 2 are then mapped to regions 3–6 by rotation about vertex 1. Coordinates in region 6 are then mapped to region 7 by rotation about vertex 2. Similarly, regions 8–11 are filled by rotating coordinates in region 7 about vertex 1. Finally, the sphere is fully coated by symmetrically equivalent atoms after region 11 is rotated about vertex 7 to fill region 12. Thus the trail of operations is

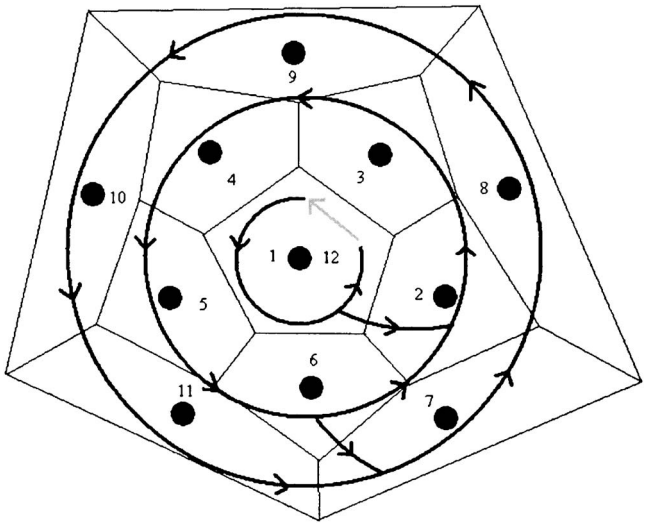

FIG. 20. Vertex graph showing the procedure used to combine the reflection and rotation operations on the sphere without degeneracy.

indicated by the directional arrows in Fig. 20 and labeled in order of occurrence by the vertex numbers.

All of the combined operations in the previous paragraph can be represented in the same form as Eq. (A8) by Eq. (A12):

$$\hat{\mathbf{S}}\mathbf{s} = \hat{R}(\theta_1,\mathbf{v}_7)\sum_{k=1}^{5}\hat{R}(\theta_k,\mathbf{v}_1)\hat{R}(\theta_1,\mathbf{v}_2)\sum_{\mathrm{j}=1}^{5}\hat{R}(\theta_{\mathrm{j}},\mathbf{v}_1)\hat{R}(\theta_1,\mathbf{v}_3) \times\sum_{\mathrm{i}=1}^{5}\hat{R}(\theta_{\mathrm{i}},\mathbf{v}_1)\{\hat{F}(\mathbf{v}_1,\mathbf{v}_3)+\hat{I}\}\begin{bmatrix}x'\\y'\\z'\end{bmatrix} \tag{A12}$$

where $\hat{I}$ is the identity operator and the total number of operations in Eq. (A12) reduces from 120 down to 60 if the reflection operator $\hat{\mathbf{F}}(\mathbf{v}_{\mathrm{i}},\mathbf{v}_{\mathrm{j}})$ is omitted, which removes the black curves from Fig. 5. It is to be also understood that Eq. (A12) requires centering of the coordinate system describing $\mathbf{s}(x,y,z)$ during the application of $\hat{\mathbf{S}}$ so that the coordinates x',y', and z' range between $-T/2$ and $T/2$ instead of between 0 and $T<R$.

Symmetry imposed on the inverted torus

Even without the curves shown in Fig. 6, it is much easier to visualize possible symmetries for the inverted torus. After shifting the origin of the coordinate system to the geometric center of the inverted torus, the symmetries shown in Fig. 6 can be described by fourfold rotation about the z axis plus reflections through the x-z and y-z planes and finally reflection about the x-y plane. Including the coordinate system origin shift, these combined operations (without degeneracy) can again be represented in a single expression:

$$\hat{\mathbf{S}}\mathbf{s} = \sum_{\mathrm{j}=0}^{1}\sum_{\mathrm{t}=0}^{1}\sum_{\mathrm{i}=1}^{4}\begin{bmatrix}0\\0\\\mathrm{Tt}\end{bmatrix}+\begin{bmatrix}1&0&0\\0&1&0\\0&0&1-2\mathrm{t}\end{bmatrix}\left(\begin{bmatrix}T/2\\T/2\\T/2\end{bmatrix}+\frac{\mathrm{j}T}{2}\begin{bmatrix}1-\cos(\mathrm{i}\pi)\\\cos(\mathrm{i}\pi)-1\\0\end{bmatrix}+\begin{bmatrix}\mathrm{j}\cos(\mathrm{i}\pi)-1&0&0\\0&1-\mathrm{j}\cos(\mathrm{i}\pi)&0\\0&0&1\end{bmatrix}\times\begin{bmatrix}\cos(2\pi/\mathrm{i})&\sin(2\pi/\mathrm{i})&0\\-\sin(2\pi/\mathrm{i})&\cos(2\pi/\mathrm{i})&0\\0&0&1\end{bmatrix}\begin{bmatrix}x-T/2\\y-T/2\\z-T/2\end{bmatrix}\right) \tag{A13}$$

where each operation on the coordinates of **s** labeled by the summation variables generates a symmetrically equivalent replica of the atom at $\mathbf{s}(x,y,z)$.

[1] S. Dimovski, J. A. Libera, and Y. Gogost, MRS Symposia Proceedings No. 706 (Materials Research Society, 2002), Z6.27.1.
[2] A. Sarkar, M. Endo, and H. W. Kroto, Carbon **33**, 5 (1995).
[3] S. Rotkin and Y. Gogotsi, Mater. Res. Innovations **5**, 191 (2002).
[4] P. J. F. Harris, A. Burian, and S. Duber, Philos. Mag. Lett. **80**, 381 (2000).
[5] P. J. F. Harris, Philos. Mag. **84**, 3159 (2004).
[6] H. Terrones, M. Terrones, and J. L. Moran-Lopez, Curr. Sci. **81**, 1011 (2001).
[7] H. Terrones and M. Terrones, New J. Phys. **5**, 126.1 (2003).
[8] D. Vanderbilt, J. Tersoff, Phys. Rev. Lett. **68**, 511 (1992).
[9] S. J. Townsend, T. J. Lenosky, D. A. Muller, C. S. Nichols, and V. Elser, Phys. Rev. Lett. **69**, 921 (1992).
[10] T. Lenosky, X. Gonze, M. Teter, and V. Elser, Nature **355**, 333 (1992).
[11] H. Terrones and A. L. Mackay, Prog. Cryst. Growth Charact. Mater. **34**, 25 (1997).
[12] A. L. Mackay and H. Terrones, Philos. Trans. R. Soc. London, Ser. A **343**, 113 (1993).
[13] M. O'Keeffe, G. B. Adams, and O. F. Sankey, Phys. Rev. Lett. **68**, 2325 (1992).
[14] H. Terrones, J. Fayos, and J. L. Aragon, Acta Metall. Mater. **42**, 2687 (1994).
[15] M. Terrones, W. K. Hsu, J. P. Hare, D. R. M. Walton, H. W. Kroto, and H. Terrones, Philos. Trans. R. Soc. London, Ser. A, **354**, 2025 (1996).
[16] H. Terrones, and M. Terrones, Phys. Rev. B **55**, 9969 (1997).
[17] H. Terrones, and M. Terrones, Fullerene Sci. Technol. **6**, 751 (1998).
[18] J. K. Johnson, B. N. Davidson, M. R. Pederson, and J. Q. Broughton, Phys. Rev. B **50**, 17575 (1994).
[19] L. Yang, J. Jiang, and J. Dong, Phys. Status Solidi B **238**, 115 (2003).
[20] R. Nesper, K. Vogel, and P. E. Blochl, Angew. Chem., Int. Ed. Engl. **32**, 701 (1993).
[21] R. Nesper, S. Leoni, ChemPhysChem **2**, 413 (2001).
[22] S. T. Hyde, S. Ramsden, T. Di Matteo, and J. J. Longdell, Solid State Sci. **5**, 35 (2003).
[23] A. Maiti, C. J. Brabec, and J. Bernholc, Phys. Rev. Lett. **70**, 3023 (1993).
[24] S. J. Townsend, T. J. Lenosky, D. A. Muller, C. S. Nichols, and V. Elser, Phys. Rev. Lett. **69**, 921 (1992).
[25] V. Rosato, M. Celino, S. Gaito, and G. Benedek, Comput. Mater. Sci. **20**, 387 (2001).
[26] V. Rosato, M. Celino, G. Benedek and S. Gaito, Phys. Rev. B **60**, 16928 (1999).
[27] R. Phillips, D. A. Drabold, T. Lenosky, G. B. Adams, and O. F. Sankey, Phys. Rev. B **46**, R1941 (1992).
[28] M. Z. Huang, W. Y. Ching, and T. Lenosky, Phys. Rev. B **47**, 1593 (1993).
[29] H. Aoki, M. Koshino, D. Takeda, H. Morise, and K. Kuroki, Phys. Rev. B **65**, 035102 (2001).
[30] N. Park, M. Yoon, S. Berber, J. Ihm, E. Osawa, and D. Tomanek, Phys. Rev. Lett. **91**, 237204 (2003).
[31] F. Valencia, A. H. Romero, E. Hernández, M. Terrones, and H. T. Errones, New J. Phys. **5**, 123.1 (2003).
[32] S. T. Hyde, and M. O'Keefe, Philos. Trans. R. Soc. London, Ser. A, **354**, 1999 (1996).
[33] A. A. Zakhidov, R. H. Baughman, Z. Iqbal, C. Cui, I. Khayrullin, S. O. Dantas, J. Marti, and V. G. Ralchenko, Science **282**, 897

(1998).
[34] R. Ryoo, S. H. Joo, and S. Jun, J. Phys. Chem. B **103**, 7743 (1999).
[35] S. Jun, S. H. Joo, R. Ryoo, M. Kruk, M. Jaroniec, Z. Liu, T. Ohsuna, and O. Terasaki, J. Am. Chem. Soc. **122**, 10712 (2000).
[36] S. H. Joo, S. Jun, and R. Ryoo, Microporous Mesoporous Mater. **153**, 44 (2001).
[37] S. B. Yoon, J. Y. Kim, and J. S. Yu, Chem. Commun. (Cambridge) **2001**, 559.
[38] L. A. Solovyov, V. I. Zaikovskii, A. N. Shmakov, O. V. Belousov, and R. Ryoo, J. Phys. Chem. B **106**, 12198 (2002).
[39] L. A. Solovyov, A. N. Shmakov, V. I. Zaikovskii, S. H. Joo, and R. Ryoo, Carbon **40**, 2477 (2002).
[40] E. Barborini, P. Piseri, P. Milani, G. Benedek, C. Ducati and J. Robertson, Appl. Phys. Lett. **81**, 3359 (2002).
[41] G. Benedek, H. Vahedi-Tafreshi, E. Barborini, P. Piseri, P. Milani, C. Ducati, and J. Robertson, Diamond Relat. Mater. **12**, 768 (2003).
[42] A. T. Balaban, Comput. Math. Appl. **17**, 397 (1989)
[43] H. W. Kroto, Comput. Math. Appl., **17**, 417 (1988).
[44] A. L. Mackay, and H. Terrones, Philos. Trans. R. Soc. London, Ser. A, **343**, 113 (1993).
[45] R. Bruce King, Croat. Chem. Acta **73**, 993 (2000).
[46] R. Bruce King, Croat. Chem. Acta **75**, 447 (2002).
[47] D. Donadio, L. Colombo, P. Milani, and G. Benedek, Phys. Rev. Lett. **83**, 776 (1999).
[48] M. Acharya, M. S. Strano, J. P. Mathews, S. J. L. Billinge, V. Petkov, S. Subramoney, and H. C. Foley, Philos. Mag. B **79**, 1499 (1999).
[49] A. Fogden, and S. T. Hyde, Acta Crystallogr., Sect. A: Found. Crystallogr. **A48**, 442 (1992).
[50] S. Lidin, S. T. Hyde, and B. W. Ninham, J. Phys. (France) **51**, 801 (1989).
[51] S. T. Hyde, Z. Kristallogr. **187**, 165 (1989).
[52] D. Plewczyński, and R. Hołyst, Physica A **295**, 371 (2001).
[53] R. Holyst, D. Plewczynski, A. Aksimentiev, and K. Burdzy, Phys. Rev. E **60**, 302 (1999).
[54] M. Wohlgemuth, N. Yufa, J. Hoffman, and E. L. Thomas, Macromolecules **34**, 6083 (2001).
[55] P. E. Harper, and S. M. Gruner, Eur. Phys. J. E **2**, 217 (2000).
[56] H. A. Schwartz, *Gesamemelte Mathematische Abhandlungen* (Springer, Berlin, 1890).
[57] D. J. Tildesley, and M. P. Allen, *Computer Simulation of Liquids* (Oxford Science, Oxford, 1987).
[58] J. F. Justo, M. Z. Bazant, E. Kaxiras, V. V. Bulatov, and S. Yip, Phys. Rev. B **58**, 2539 (1998).
[59] N. A. Marks, Phys. Rev. B **63**, 035401 (2000).
[60] N. A. Marks, J. Phys.: Condens. Matter **14**, 2901 (2002).
[61] M. Terrones, F. Banhart, N. Grobert, J. C. Charlier, H. Terrones, and P. M. Ajayan, Phys. Rev. Lett. **89**, 075505 (2002).
[62] M. Wilson, K. Kannangara, G. Smith, M. Simmons, and B. Raguse, *Nanotechnology: Basic Science and Emerging Technology*, (UNSW press, 2002).
[63] D. S. Franzblau, Phys. Rev. B **44**, 4925 (1991).
[64] G. B. Arfken and H. J. Weber, *Mathematical Methods for Physicists* (Harcourt/Academic Press, New York, 2001).
[65] D. B. Litvin, Acta Crystallogr., Sect. A: Found. Crystallogr. **A47**, 70 (1991).